

# Elemental Anisotropic Growth and Atomic-Scale Structure of Shape-Controlled Octahedral Pt–Ni–Co Alloy Nanocatalysts

Rosa M. Arán-Ais,<sup>†</sup> Fabio Dionigi,<sup>‡</sup> Thomas Merzdorf,<sup>‡</sup> Martin Gocyla,<sup>§</sup> Marc Heggen,<sup>§</sup> Rafal E. Dunin-Borkowski,<sup>§</sup> Manuel Gliech,<sup>‡</sup> José Solla-Gullón,<sup>†</sup> Enrique Herrero,<sup>†</sup> Juan M. Feliu,<sup>\*,†</sup> and Peter Strasser<sup>\*,‡</sup>

<sup>†</sup>Instituto de Electroquímica, Universidad de Alicante, Apartado 99, 03080 Alicante, Spain

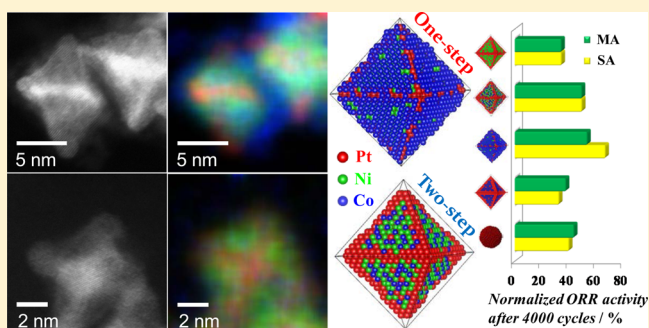
<sup>‡</sup>The Electrochemical Energy, Catalysis, and Materials Science Laboratory, Department of Chemistry, Chemical Engineering Division, Technical University Berlin, 10623 Berlin, Germany

<sup>§</sup>Ernst Ruska-Centre for Microscopy and Spectroscopy with Electrons, Forschungszentrum Jülich GmbH, 52425 Jülich, Germany

## Supporting Information

**ABSTRACT:** Multimetallic shape-controlled nanoparticles offer great opportunities to tune the activity, selectivity, and stability of electrocatalytic surface reactions. However, in many cases, our synthetic control over particle size, composition, and shape is limited requiring trial and error. Deeper atomic-scale insight in the particle formation process would enable more rational syntheses. Here we exemplify this using a family of trimetallic PtNiCo nanooctahedra obtained via a low-temperature, surfactant-free solvothermal synthesis. We analyze the competition between Ni and Co precursors under coreduction “one-step” conditions when the Ni reduction rates prevailed. To tune the Co reduction rate and final content, we develop a “two-step” route and track the evolution of the composition and morphology of the particles at the atomic scale. To achieve this, scanning transmission electron microscopy and energy dispersive X-ray elemental mapping techniques are used. We provide evidence of a heterogeneous element distribution caused by element-specific anisotropic growth and create octahedral nanoparticles with tailored atomic composition like Pt<sub>1.5</sub>M, PtM, and PtM<sub>1.5</sub> (M = Ni + Co). These trimetallic electrocatalysts have been tested toward the oxygen reduction reaction (ORR), showing a greatly enhanced mass activity related to commercial Pt/C and less activity loss than binary PtNi and PtCo after 4000 potential cycles.

**KEYWORDS:** PtNiCo octahedra, intraparticle composition, anisotropic growth, oxygen reduction reaction



Over the past years, extensive research and development has been carried out in fuel cells with the aim of implementing this technology on transportation, stationary, and portable power generation.<sup>1,2</sup> Nevertheless, some issues such as catalysts' kinetic limitations, durability, and cost must still be addressed before their successful commercialization. Oxygen reduction electrocatalysts are known to play a crucial role on fuel cells performance, being the fundamental studies on the subject still required to overcome these barriers.<sup>3,4</sup> By alloying Pt with other non-noble metals, it is possible to produce cheaper electrocatalysts with novel properties for the oxygen reduction reaction (ORR) due to lattice compression<sup>5,6</sup> and/or modified electronic properties.<sup>7,8</sup> Thus, several studies have shown that binary Pt-M (M = Cr, Mn, Fe, Co, Ni, Cu, V, Ti) nanocrystals (NCs) greatly enhanced the kinetics of the ORR in comparison with standard Pt catalysts.<sup>9–11</sup> However, besides the composition, the intrinsic activity of nanoparticles also depends on their size and shape which strongly determine the atomic surface structure of the nanoparticles.<sup>12–15</sup> Thus, by controlling the morphology of the NCs, it is possible to

maximize the exposure of certain facets that exhibit better catalytic properties.<sup>16,17</sup> These are the premises that led to establish {111}-Pt<sub>3</sub>Ni surfaces as the ideal electrocatalyst for the ORR.<sup>18,19</sup> Since then, many synthetic routes to obtain PtNi nanooctahedra, which ideally exhibit eight facets with {111} atomic arrangement, have been developed, in which the coreduction of the metal precursors takes place in the solution phase.<sup>20–24</sup> A recent study<sup>25</sup> has shed light onto the growth mechanism of binary PtNi octahedral nanoparticles, revealing an anisotropic growth where a Pt-rich phase first develops into hexapod-like concave NCs in a ligand-controlled kinetic process, followed by a layer-by-layer deposition of a Ni-rich phase at the concave {111} facets. The degradation pathway of these nanocatalysts in acidic media<sup>25,26</sup> showed the selective etching of the Ni-rich {111} facets, which first results in the formation of concave nanooctahedra and finally in Pt-rich

Received: August 2, 2015

Revised: September 29, 2015

Published: October 6, 2015

skeleton frameworks. These frameworks have less active facets, such as {110} and {100}, and therefore an activity decay is observed after thousands of potential sweeping cycles. According to the complex anisotropic structure formation of bimetallic octahedral nanoparticles, an increase of the stability of these materials seems to be very challenging. The incorporation of a third metal to the shaped PtNi nanoparticles (the best known so far electrocatalysts for ORR<sup>23,27</sup>) can provide a strategy to improve their stability. Ideally, the electronic effect of a second transition metal would further fine-tune the d-band center of Pt, thus facilitating the kinetics of the reaction and preventing or slowing nickel dissolution at the same time. In addition, stability against degradation by dealloying can be increased by a more negative heat of formation. Pt<sub>3</sub>Co has been reported having more negative enthalpy of formation than Pt<sub>3</sub>Ni,<sup>28</sup> suggesting a possible higher stability. Furthermore, the entropic negative contribution to the Gibbs free energy of mixing for the ternary system respect to the two binaries will favorably contribute to stability. So a number of reports have dealt with Pt-based ternary alloy nanoparticles for ORR,<sup>29–31</sup> but none has put effort in tailoring their morphological shape.<sup>32–34</sup> Now, on the basis of previous studies, Pt–Co binary alloy catalysts also exhibit high activity and stability,<sup>35–38</sup> and for that reason, spherical PtNiCo ternary alloys have attracted more attention as a family of ORR catalysts that would allow tuning both ORR activity and stability.<sup>39–42</sup> However, synthetic control of their shape and composition as well as atomic-scale knowledge and control over the spatial distribution of the metal atoms across the NCs has remained elusive. There exists a challenging knowledge gap on the evolution of ternary shaped materials at the nanoscale and their rational synthesis. We address this critical issue here.

We investigate the synthesis, structure, and reactivity of shape-controlled octahedral PtNiCo nanoparticle catalysts, with particular emphasis on their anisotropic growth patterns. In practical terms, this study analyzes preparation routes, associated morphology, elemental distributions, and the chemical state of active and stable shaped ternary ORR catalysts. However, more importantly, our study provides new exemplary insights in the growth processes of ternary shaped particles in general. As such, it aids the development of more rational knowledge-based preparation routes for other ternary NCs. More specifically, we highlight an element-specific competition in reductive deposition of the different metals during a low-temperature solvothermal growth process of NCs.<sup>21</sup> The amount of metal precursors and/or the reaction stage in which they are added controls the size, shape, and the intraparticle composition. To the best of our knowledge, there are no previous reports addressing the evolution of elemental anisotropy in shaped ternary alloy nanoparticles.

Trimetallic PtNiCo shape-controlled nanoparticles were prepared using a surfactant-free, low-temperature solvothermal synthesis.<sup>21,25,26,43</sup> In one synthesis, henceforth referred to as “one pot approach”, Pt(acac)<sub>2</sub>, Ni(acac)<sub>2</sub>, and Co(acac)<sub>2</sub> were simultaneously reduced in *N,N*-dimethylformamide (DMF) at 130 °C for 42 h. The molar amount and ratio of the Pt and Ni precursors were fixed (Pt:Ni ratio = 1:2.5), while the amount of Co precursor was gradually increased from 0 to 5.0 mmol (Table S1). The as-prepared nanoparticles were supported on carbon and washed several times with ethanol/water mixtures. The atomic composition of these samples, determined by inductively coupled plasma mass spectroscopy (ICP-MS), is shown in Figure 1A as a function of the initial amount of Co. At

130 °C, a very large amount of Co precursor was needed to achieve a final Co content of up to 20%. In addition, the ratio Ni:Pt in the nanoparticles with low Co content is close to 1, indicating that the reduction rate of Ni (that is in higher concentration) was slower than that of Pt. By adding 6 times more Co than Ni precursors, it was possible to obtain nanoparticles with a Pt<sub>31</sub>Ni<sub>51</sub>Co<sub>18</sub> composition, pointing out a very slow reduction rate of Co in comparison with Pt and Ni. In addition, our results suggest that this reduction rate was limited for a high Co precursor content, since with the addition of more Co precursor (10 times more Co than Ni), the Co content in the nanoparticles remained essentially constant (Pt<sub>31</sub>Ni<sub>50</sub>Co<sub>19</sub>). Interestingly, the Ni:Pt ratio increased with the Co content of the nanoparticles (Figure S1). The main contribution to the Ni:Pt increase is due to the decrease of the percentage composition of Pt in the nanoparticle. Since Pt is expected to be almost fully reduced at this temperature and a decrease of its reduction rate is unlikely, we propose that an increase in the reduction rate of Ni occurs with increasing initial Co amount.

Figures 1B and C show the atomic compositions of nanoparticles synthesized at 160 and 200 °C, respectively, for different amounts of Co precursor. The synthesis temperature was now raised in order to increase the amount of Co in the nanoparticles. At intermediate temperature (160 °C), Ni is largely reduced, with the atomic percentage of Ni and Pt in the nanoparticles being almost independent of the initial amount of Co. However, when the synthesis was performed at higher temperature (200 °C), the three metals were completely reduced, leading to a final atomic composition very close to the initial percentage of precursors added.

Figures S2A and S2B show the compositional trends for the three metals (Pt, Ni, and Co) as a function of heating temperature. The Ni content strongly increases with the temperature from 130 to 160 °C, due to an enhancement in the Ni reduction rate. On the other hand, the reduction rate of Co improves significantly only at 200 °C, as can be seen in Figure 2C, while at 130 and 160 °C, the Co content is essentially similar.

Figure 1D shows a representative set of X-ray diffraction (XRD) patterns of the samples synthesized at 130 °C. The diffraction peak positions of the ternary alloys fall in between those of monometallic Pt and those for monometallic Ni and Co, which demonstrates the presence of a single-crystalline structure for all the compositions and which reflect the bulk alloy phase of the PtNiCo obtained at this temperature. All NCs showed Bragg reflections ascribed to a face-centered cubic (fcc) structure, with peaks shifting to higher 2θ values as the content in Ni and Co is increased. Alloying Pt with elements of smaller atomic radius such as Co and Ni reduces the interatomic distances near the Pt sites, thus producing a contraction of the atomic lattice and a shift of the peak positions toward higher angles. Note that the peaks become progressively broader as the initial amount of Co precursor added is raised. Since the peak broadening can be related to the particle size (Scherrer equation),<sup>44</sup> one possible explanation to this broadening is that the particle size of these electrocatalysts decreases as their non-noble metals content increases. Particle size distributions corroborate this aspect, even though the decrease is small [14.0 ± 2.4 nm (Pt<sub>36</sub>Ni<sub>58</sub>Co<sub>6</sub>) versus 12.9 ± 2.7 nm (Pt<sub>30</sub>Ni<sub>51</sub>Co<sub>19</sub>)]. However, it should be stressed that dealloying of Co may also contribute to the peak broadening. The small asymmetry observed for the (200) peak may also

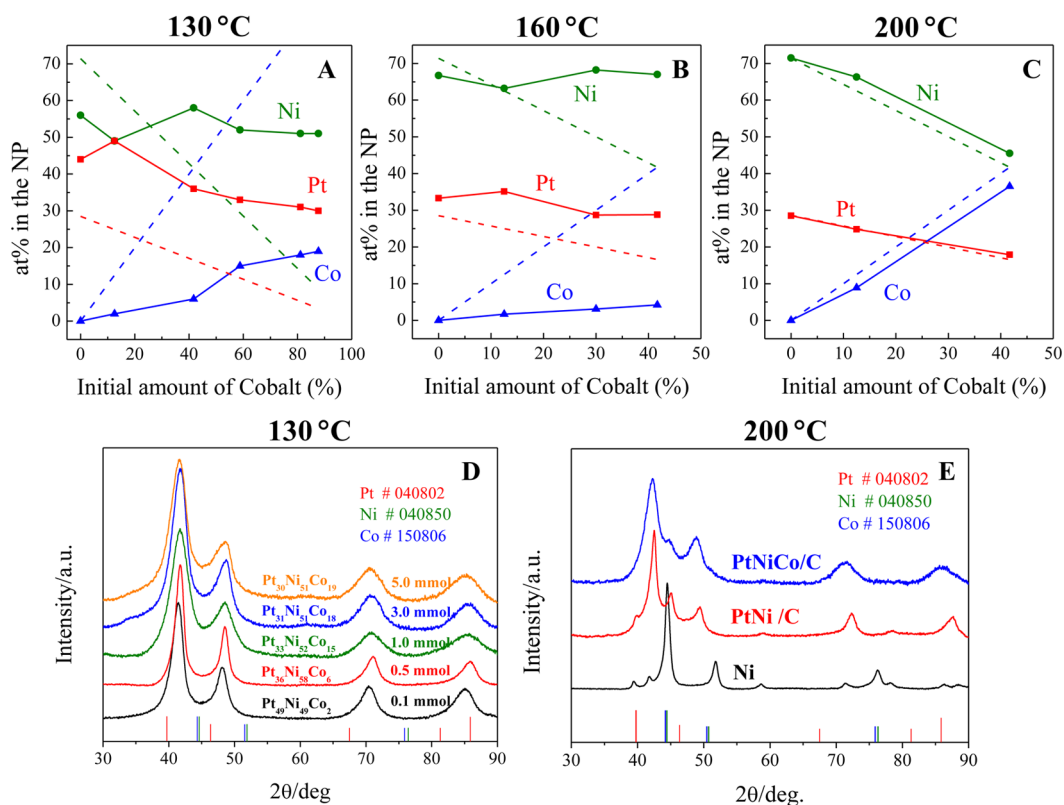


**Figure 1.** (A–C) Atomic compositions of the trimetallic nanoparticles synthesized at 130, 160, and 200 °C, respectively. Dashed lines correspond to the expected composition if the entire precursor is reduced. XRD patterns of (D) PtNiCo octahedral nanoparticles synthesized at 130 °C and (E) trimetallic, bimetallic, and pure Ni nanoparticles obtained at 200 °C are presented.

support this effect. The dealloying Co in PtNiCo octahedra in the case of high Co content will be discussed more in detail in the following.

The XRD patterns of both binary and ternary nanoparticles obtained at higher temperature (Figure 1E) show the emergence of a secondary phase pointing out the presence of the metal phases of individual elements. Although the reduction of the three metals is almost complete at 200 °C, the synthesis at this high temperature is discarded since it leads to an undesirable condition (non alloyed nanoparticles). For that reason, we propose that PtNiCo nanoparticles with a maximum content of about 19 % in Co can be obtained by our “one-step” synthesis when the initial amount of the Co precursor is chosen 10 times higher than that of the Ni precursor (Table S1).

Figure 2 presents a microstructural analysis of the Pt<sub>30</sub>Ni<sub>51</sub>Co<sub>19</sub> nanoparticles synthesized by the “one-step” method using high-angle annular dark field scanning transmission electron microscopy (HAADF-STEM). The particles have an octahedral shape, and an average size (estimated by the longest length connecting two opposite vertices) of 12.9 ± 2.7 nm (Figure 2A–C). This particle size is slightly larger than that reported for binary PtNi octahedra (12 ± 0.8 nm) synthesized with the same concentration of Ni and Pt precursors and similar to that found with PtNi<sub>1.5</sub> octahedra (13 ± 1.2 nm), synthesized with larger excess of Ni precursors, reported in the same study.<sup>26</sup> The energy dispersive X-ray (EDX) elemental mapping, Figure 2D, shows a heterogeneous distribution of the three elements throughout the particles. The distribution of Pt and Ni is consistent with previous findings<sup>25,26</sup> where a Pt enrichment was found at the corners and edges, while Ni is present at the {111} facets of the

nanooctahedra. The EDX elemental mapping of the ternary alloy nanooctahedra in Figure 2 shows a Pt-rich skeleton (red) and a high content of Ni (green) on the facets. Co (blue) is mainly present at the outer surface rather than in the inner part of the nanoparticles. The EDX analysis shows a composition of Pt<sub>17</sub>Ni<sub>50</sub>Co<sub>33</sub> for the left nanoparticle in Figure 2D and Pt<sub>18</sub>Ni<sub>52</sub>Co<sub>30</sub> for the nanooctahedron on the right. These results exhibit higher non-noble metal content, particularly in the case of Co, in comparison with those obtained from ICP-MS, pointing out that the extensive washing procedure of the supported nanoparticles for ICP and electrochemical testing leads to a partial loss of Co and Ni present at the surface in comparison with the samples for EDX investigations which were taken from the colloidal suspension after the DMF removal. The anisotropic distribution of both non-noble metals (Co mainly located at the surface of the nanoparticles and Ni being present in the center of the facets) drives to a removal of these elements in a different extension after washing procedure, thus leading to different Pt:Ni ratios. Five-twinned nanoparticles with decahedral shape were also found during the microscopic analysis (Figure S3). These results, in combination with the detailed ICP-MS and EDX analysis of the atomic composition of the different samples synthesized, lead us to hypothesize an element-specific anisotropic growth of the shaped trimetallic nanoparticles, where the Pt reduces first forming an hexapod-like structure, followed by a further reduction of Pt and Ni onto the {111} facets. The slow reduction rate of Co precludes or decreases not only its incorporation into the core of the nanoparticles, but also its reduction on the Ni-rich PtNi facets. In fact, even at high concentration, Co would only be found preferentially on the

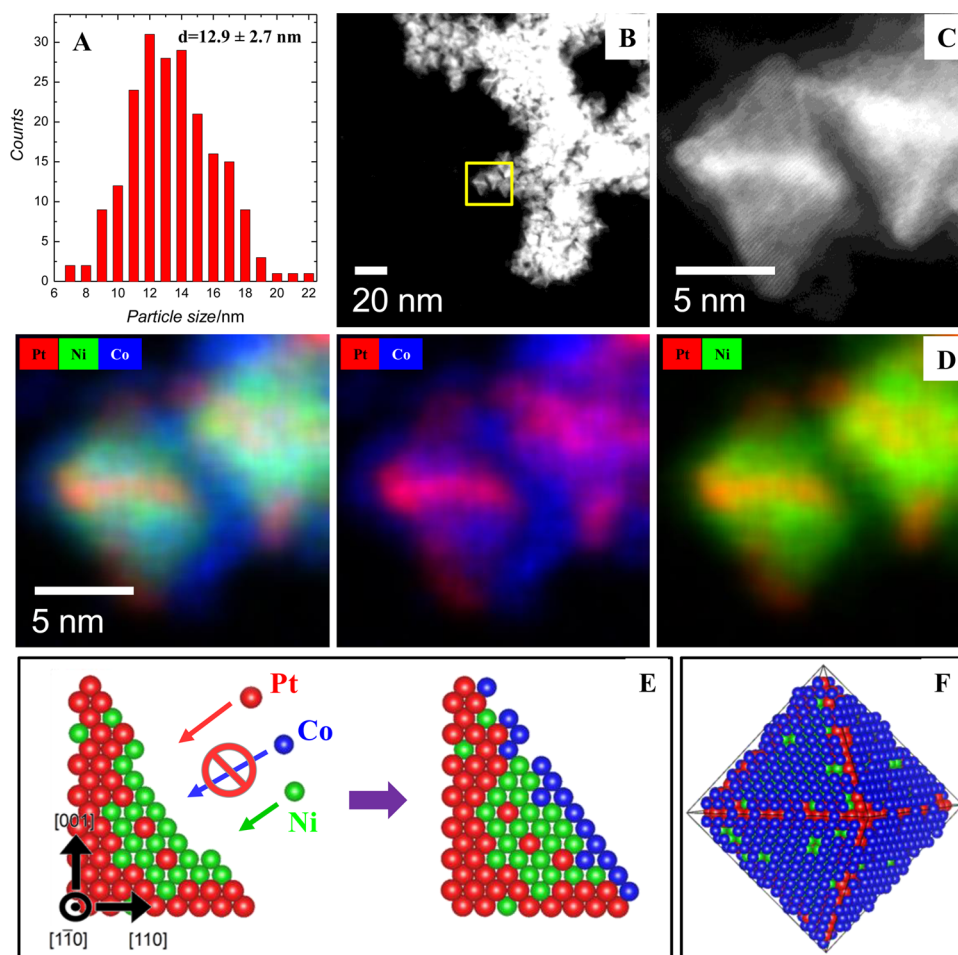


**Figure 2.** Morphology and composition analysis of octahedral PtNiCo nanoparticles synthesized in a one-step solvothermal synthesis process. (A) Particle size distribution. Representative HAADF-STEM images at (B) low and (C) high magnification of the PtNiCo nanocrystals. (D) Distribution of Pt (red), Ni (green), and Co (blue) in EDX composition maps for octahedral nanoparticles. (E) Scheme proposed for the growth of the PtNiCo octahedral nanoparticles in the “one-step” synthesis and (F) 3D representation of the nanocrystals obtained.

surface of the nanoparticles. The proposed growth mechanism is schematized in Figure 2E. Figure 2F shows a 3D representation of the octahedral PtNiCo nanoparticles obtained by the “one-step” synthesis.

Our current findings indicate that kinetics play against the incorporation of Co into the core of the nanoparticles during coreduction conditions. Nevertheless, it has been reported that obtaining PtCo nanoparticles with an octahedral shape is possible.<sup>25</sup> In addition, our results from the “one-step” synthesis point out that the Co reduction is inhibited by the presence of Ni.

In order to overcome these limitations of the “one-step” synthesis, we developed another synthesis route where Pt and Co simultaneously reduce in the first stage of the growth process and Ni is added in a second step of the process. In this “two-step” synthesis, a Pt-rich-Co hexapod would be formed first, where most likely in agreement with previous studies, some Co can start depositing on the not yet formed {111} facets (Figure 3A).

An optimal length of time of a first growth step ( $t_1$ ) in which the coreduction of Pt and Co precursors (in a 1:2.5 ratio) takes place, and optimal length of time ( $t_2$ ) of a subsequent step during which the added Ni salt (same amount of Co precursor) is coreduced, totaling ( $t_1 + t_2$ ) about 42 h. Based on this case, variations in step durations ( $t_1/t_2$ ) from 16 h/26 to 24 h/18 h

and to 32 h/10 h yielded nanoparticles including shaped octahedra with atomic compositions of  $\text{Pt}_{69}\text{Ni}_{27}\text{Co}_4$ ,  $\text{Pt}_{48}\text{Ni}_{27}\text{Co}_{25}$ , and  $\text{Pt}_{55}\text{Ni}_8\text{Co}_{37}$  and with particle sizes of  $6.9 \pm 1.1$ ,  $9.9 \pm 1.5$ , and  $8.3 \pm 1.4$  nm, respectively. TEM images (Figure S4) of the as-prepared nanoparticles show that in all cases octahedral nanoparticles can be obtained, the 24 h/18 h synthesis being the one that produces the highest yield of nanooctahedra. Since the total duration of the synthesis is the same for all the samples, it would be expected to obtain NCs with a similar particle size. Nevertheless, the final dimension and morphology of the nanoparticles seemed to be both determined by the duration of the binary coreduction of Pt and Co and the later ripening stage in the presence of Ni. The XRD patterns (Figure S5) show the presence of a single crystalline phase (alloyed nanoparticles) in all samples. The diffraction peaks shift to higher  $2\theta$  angle as the content in non-noble metals of the nanocatalysts is increased. For the shortest  $t_1$ , smaller Pt-rich nanoparticles with octahedral shape are obtained. On the other hand, for the longest  $t_1$ , corner-rounded octahedra with low content in Ni are prevalent. Well-defined nanooctahedra are collected for the intermediate  $t_1$  tested, with a 2:1:1 Pt:Ni:Co ratio in the final atomic composition.

Figure 3A shows the scheme followed in the “two-step” synthesis, where the 3D models represent the rational design of the synthetic route. HAADF-STEM images of octahedral

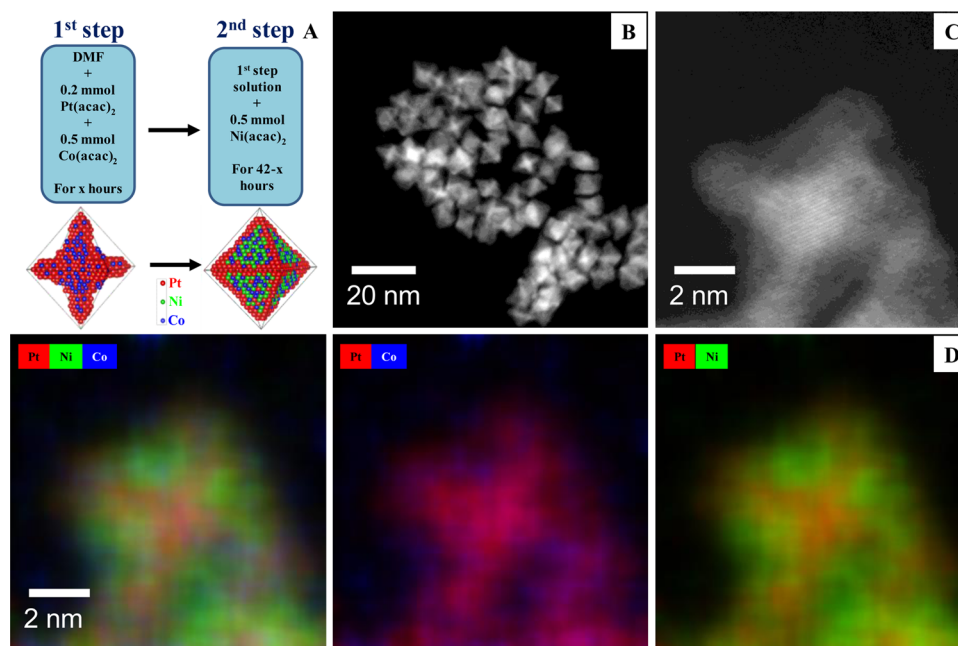


**Figure 3.** Morphology and composition analysis of octahedral PtNiCo nanoparticles synthesized in two steps. (A) Scheme of the two-step synthesis and possible model for the formation of the trimetallic nanoparticles. Representative HAADF-STEM images at (B) low and (C) high magnification of the PtNiCo nanocrystals. (D) EDX elemental mapping of nanoparticle in (C): Pt (red), Ni (green), Co (blue).

nanoparticles obtained using the optimized combination of synthesis times (24 h/18 h) are shown in Figures 3A and B. The EDX composition maps (Figure 3D) of a selected octahedral nanoparticle clearly shows the presence of Co both in the inner and outer parts of the nanoparticles. These images suggest the formation of ternary alloyed nanoparticles consisting of a Pt-rich skeleton (red, mainly present on the hexapod-like structure), Ni-rich {111} facets, and Co (blue) distributed throughout the nanoparticle. Although ICP-MS results suggest that the “two-step” synthesis leads to PtNiCo nanoparticles with a higher Co atomic composition than the “one-step” synthesis, the EDX analysis of the obtained nanooctahedra show an average composition of  $\text{Pt}_{40}\text{Ni}_{50}\text{Co}_{10}$ . The higher content in Co of the ICP-MS measurements is derived from the presence of spherical PtCo-rich nanoparticles in the sample (Figure S6). The elemental mapping shows that Ni and Co are more homogeneously distributed at the {111} facets than in the case of the nanoparticles obtained in the “one-step” synthesis. A comparison of the Co-distribution by EDX after the one-step and two-step synthesis is shown in Figure S7.

Following the “two-step” synthesis and using the optimized times 24 h/18 h, we attempted to synthesize nanoparticles with a controlled composition, always trying to keep the octahedral shape. The adsorption of the DMF-solvated acetylacetonate ligand on the {111} surfaces allows the growth of the nanocrystals along the  $\langle 100 \rangle$  direction and thus the formation of hexapods-like structures. Pt-rich octahedral nanoparticles synthesized by the “two-step” process were obtained by adding smaller amounts of non-noble metals precursor. In order to keep the synthetic conditions constant, the shortage of the acetylacetonate ligand was supplemented by adding K(acac) in the first step of the synthesis. On the other hand, M-rich nanoparticles were synthesized by adding almost 4 times more Ni(acac)<sub>2</sub> and Co(acac)<sub>2</sub> than Pt(acac)<sub>2</sub>. The concentrations tested are summarized in Table S2. Interestingly, compositions

like  $\text{Pt}_{1.5}\text{M}$ , PtM, and  $\text{PtM}_{1.5}$  can be obtained by using M:Pt ratios of 2:0.8, 4:0.8, and 6:0.8, respectively. Figure S8 shows the TEM images and the size distribution of the nanoparticles synthesized. As can be seen, a high yield of well-defined Pt-rich nanooctahedra can be obtained using this synthetic reaction (Figure S8A). These particles appear to have a bigger diameter from edge to edge in comparison with PtM nanoparticles (Figure S8B). This fact might be due to the partial substitution of Co(acac)<sub>2</sub> precursor with K(acac) precursor, which might promote the growth of larger Pt-rich hexapods in the initial phases of the synthesis. However, further experiments are necessary to clarify this point. We can find the opposite situation when the synthetic reaction is performed in a non-noble metal-rich medium. Figure S8C shows a variety of nanoparticles with different shapes and wide size distribution. Octahedral nanocrystals can be observed in the TEM images, with sizes from 12 to 22 nm approximately, surrounded by spherical nanoparticles of different dimensions. In this case, the largest coreduction of Co and Pt in the first phase might cause the nanoparticles to collapse into spherical shape. At the same time, the formation of bigger hexapod-like structures in the excess of acetylacetonate ligand followed by larger deposition of Ni onto the {111} facets could be responsible of the formation of bigger octahedra. No phase segregation was determined from the XRD patterns of these samples (Figure S9), denoting the formation of alloyed nanoparticles in all cases, regardless the yield of nanooctahedra obtained.

Finally, the electrocatalytic ORR activity of these carbon supported ternary nanoparticles was evaluated and compared with that obtained with binary octahedral PtNi/C,<sup>26</sup> PtCo/C, and commercial Pt/C electrocatalysts. Pt loadings of all binary and ternary samples including commercial Pt/C benchmarks were kept at a 20–25 wt % level. Prior to the electrocatalytic testing, the catalysts were activated using the procedure described in ref 26. The voltammetric response of these catalysts (Figure 4A) showed a Pt-like profile with somewhat

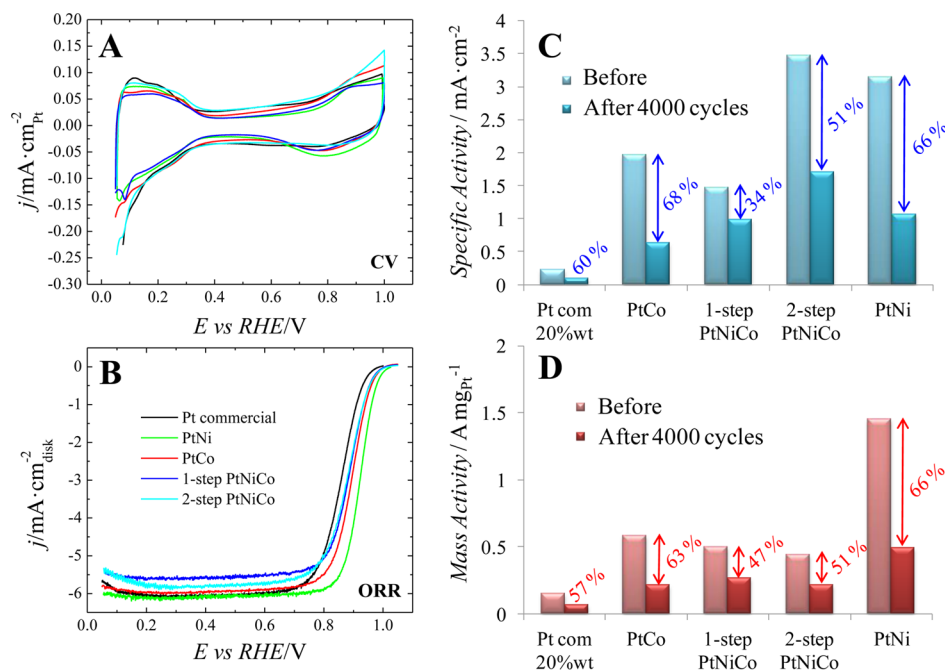


**Figure 4.** Electrochemical study of the octahedral ternary alloy nanoparticles prepared by the “one-step” and the optimized “two-step” solvothermal synthesis, relative to binary PtNi<sup>26</sup> and PtCo octahedral catalysts. (A) Cyclic voltamograms (CV) in 0.1 M HClO<sub>4</sub> (50 mV/s), normalized to H<sub>upd</sub> ECSA. (B) ORR polarization curves recorded in O<sub>2</sub>-saturated 0.1 M HClO<sub>4</sub> with a scan rate of 10 mV/s at 1600 rpm; the currents were normalized to the geometric area of the rotating disk electrode (0.196 cm<sup>2</sup>). (C, D) Specific activity and mass activity, respectively, before and after 4000 potential cycles between 0.5 and 1.0 V (vs RHE) at a sweep rate of 50 mV/s. The loss of activity after the stability test (normalized to the initial activity) is indicated. Activities were evaluated at 0.9 V (vs RHE) using the Koutecky–Levich equation.

less defined adsorption–desorption features due to the presence of Co and/or Ni on the surface.<sup>45–47</sup> The ORR polarization curves for the activated ternary alloys obtained in “one-step” and “two-step” synthesis are compared to octahedral PtCo and PtNi<sup>26</sup> catalysts and commercial Pt/C nanoparticles in Figure 4B. For each electrocatalyst, the characteristic kinetic current at 0.9 V was calculated from the ORR polarization curves using the Koutecky–Levich equation. These values were normalized to the ECSA and the Pt mass to obtain the specific and the mass activity, respectively (Figure 4C and D). The specific activities of both “one-step” and “two-step” ternary nanoparticles are about 6-fold and 15-fold higher than the state-of-the-art Pt/C catalyst at 0.9 V, respectively, together with a 3-fold enhanced mass activity for both types of trimetallic nanoparticles in comparison with commercial Pt/C (Figure 4C and D). Interestingly, the specific activity shown by the “two-step” PtNiCo electrocatalyst is higher than that obtained with the PtNi/C nanooctahedra. However, this enhancement is not reflected in the mass activity as well. Since the ECSA has been calculated from the charge involved in the H<sub>UPD</sub> region (H adsorbed onto the Pt atoms), these results suggest a M-enrichment at the surface of the “two-step” PtNiCo nanocatalyst, in comparison with PtNi electrocatalyst, where more Pt would be present at the {111} facets of the nanooctahedra. The same situation would be also expected for the “one-step” PtNiCo nanoparticles, where the EDX elemental mapping showed a surface Co-enrichment. Nevertheless, in this case, Co is preferentially attached to the Pt–Ni {111} facets and it is more easily dissolved in the acidic solution during the electrochemical testing. In fact, for inks containing the same amount of Pt, the “two-step” PtNiCo sample displayed about 3 times less ECSA (3.0 m<sup>2</sup>/g<sub>cat</sub>) than PtNi and “one-step” PtNiCo nanocatalysts (8.6 m<sup>2</sup>/g<sub>cat</sub>).

The electrochemical stability of the PtCo and PtNiCo octahedral nanoparticles was evaluated using an accelerated durability cycling test between 0.5 and 1.0 V (vs RHE) at a sweep rate of 50 mV/s in N<sub>2</sub>-saturated 0.1 M HClO<sub>4</sub>. Figure S10 shows how the voltammetric profiles of all samples evolves to the typical response of pure Pt/C, being the peaks at 0.14 and 0.26 V progressively defined by successive potential cycling. On the contrary, at potentials above 0.8 V (where OH adsorption/desorption and oxides formation take place) a decrease in the current density is observed as the number of cycles applied increases. Both facts agree with dissolution of the non-noble metals from the surface of the catalysts, producing the disappearance of the {111} facets and the formation of Pt-skeleton nanostructures. These changes of the surface composition and structure inevitably lead to a drop in the activity of these nanocatalysts. The polarization curves before and after the durability test show a negative shift of 31 mV for PtCo/C and 20 mV and 10 mV for the PtNiCo/C synthesized in one and two steps, respectively. As shown in Figures S10 G–H, the Pt mass activity of the Pt<sub>30</sub>Ni<sub>51</sub>Co<sub>19</sub> and Pt<sub>48</sub>Ni<sub>27</sub>Co<sub>25</sub> catalysts dropped 47% and 51%, respectively. Interestingly, the “two-step” PtNiCo electrocatalyst presents a higher specific activity after the durability test. Therefore, although the catalytic mass activity of ternary alloys is not as high as for bimetallic PtNi and PtCo, our results demonstrate that, by alloying Pt with Ni and Co, the loss in specific and mass activity can be reduced in comparison with carbon supported Pt, PtNi, and PtCo catalysts.

Besides the loss in activity after the stability test, we also investigated the associated structural changes of the two octahedral trimetallic catalysts after the electrochemical processing. We performed TEM analysis of both “one-step” and “two-step” PtNiCo octahedra after a durability cycling

protocol up to 2000 cycles (Figures S11 and S12). In both cases, it is possible to observe a structure modification of the octahedral shapes toward Pt skeleton structures (Pt rich hexapods and Pt terminated concave octahedral) associated with a dramatic decrease of the octahedra {111} facet area. This behavior is similar to what it has been observed in previous contribution for Ni-rich PtNi octahedra.<sup>26</sup> The non-noble metal rich octahedra will be partially leached in acid electrolyte and will result in skeleton-type structure. Thus, the dealloying process of these trimetallic catalysts under electrochemical conditions would produce Pt-rich “concave octahedral” nanoparticles through a preferential leach in their facet centers. Further leaching of the non-noble components, besides the protecting Pt skeleton, produces dendritic Pt frameworks which have less active facets, such as {110} and {100}, and therefore an activity decay is observed after thousands of potential sweeping cycles. Therefore, we conclude that the instability in both cases is due to structure changes that occur with excessive dealloying of the non-noble metals.

In conclusion, our study analyzed the growth, structure, and elemental distribution of octahedral PtNiCo nanoparticle catalysts at the atomic scale.<sup>21</sup> We observed that Co reduced more difficult in the presence of Ni, resulting in severe compositional anisotropies. To circumvent this, Co was required in large excess to obtain octahedral particles with a maximum Co content of Pt<sub>31</sub>Ni<sub>51</sub>Co<sub>18</sub>. STEM and EDX investigations showed that Co is mainly present at the surface of the nanoparticles after “one-pot” preparations. We then developed a “two-step” synthetic route requiring less Co precursor for octahedral nanocatalysts and with both Co and Ni distributed more homogeneously at the {111} facets and less anisotropy. The “two-step” synthesis finally allowed for the design of ternary nanoparticles with tuned atomic compositions ranging from Pt<sub>1.5</sub>M to PtM and PtM<sub>1.5</sub> (M = Ni + Co). The octahedral PtNiCo/C showed ORR activities with a 3-fold enhanced mass activity than commercial Pt/C and less activity loss than binary PtNi<sup>26</sup> and PtCo after 4000 potential cycles. Thus, beyond the improvement and tuning of synthetic pathways of a specific ternary Pt alloy catalyst systems with improved ORR performance, the present study suggests the importance of anisotropic growth patterns in shaped ternary Pt alloy systems in general. We believe that such insights will aid the tailoring of the bulk and surface composition and thus reactivity of octahedral Pt-based nanoparticles.

## ■ ASSOCIATED CONTENT

### Supporting Information

The Supporting Information is available free of charge on the ACS Publications website at DOI: 10.1021/acs.nanolett.5b03057.

Experimental details, tables of nanoparticles' composition, HAADF-STEM and EDX elemental maps, TEM images, graphics of particle size distribution, XRD diffractograms, stability tests (cyclic voltammograms in the supporting electrolyte and ORR polarization curves) (PDF)

## ■ AUTHOR INFORMATION

### Corresponding Authors

\*E-mail: pstrasser@tu-berlin.de.

\*E-mail: juan.feliu@ua.es.

## Notes

The authors declare no competing financial interest.

## ■ ACKNOWLEDGMENTS

P.S. acknowledges financial support by the German Research Foundation (DFG) through grant STR 596/S-1 (“Nanoscale Pt Alloy electrocatalysts with well-defined shapes”). Partial funding by the German Ministry of Education and Research (BMBF) grant “LOPLAKAT” is gratefully acknowledged. Also, this work was financially supported by the MICINN (Spain) (project 2013-44083-P). R.M.A.A. thanks the funding received from MICINN (EEBB-I-14-08240) to carry out a predoctoral stay in a foreign R&D center. M.H. thanks the Deutsche Forschungsgemeinschaft (DFG) for financial support within the grant HE 7192/1-1.

## ■ REFERENCES

- (1) Tollefson, J. *Nature* **2010**, *464*, 1262–1264.
- (2) Debe, M. K. *Nature* **2012**, *486*, 43–51.
- (3) Guo, S.; Zhang, S.; Sun, S. *Angew. Chem., Int. Ed.* **2013**, *52*, 8526–8544.
- (4) Katsounaros, I.; Cherevko, S.; Zeradjanin, A. R.; Mayrhofer, K. J. *J. Angew. Chem., Int. Ed.* **2014**, *53*, 102–121.
- (5) Prabhudev, S.; Bugnet, M.; Bock, C.; Botton, G. A. *ACS Nano* **2013**, *7*, 6103–6110.
- (6) Strasser, P.; Koh, S.; Anniyev, T.; Greeley, J.; More, K.; Yu, C.; Liu, Z.; Kaya, S.; Nordlund, D.; Ogasawara, H.; Toney, M. F.; Nilsson, A. *Nat. Chem.* **2010**, *2*, 454–460.
- (7) Stamenkovic, V.; Mun, B. S.; Mayrhofer, K. J. J.; Ross, P. N.; Markovic, N. M.; Rossmeisl, J.; Greeley, J.; Norskov, J. K. *Angew. Chem., Int. Ed.* **2006**, *45*, 2897–2901.
- (8) Stephens, I. E. L.; Bondarenko, A. S.; Perez-Alonso, F. J.; Calle-Vallejo, F.; Bech, L.; Johansson, T. P.; Jepsen, A. K.; Frydendal, R.; Knudsen, B. P.; Rossmeisl, J.; Chorkendorff, I. *J. Am. Chem. Soc.* **2011**, *133*, 5485–5491.
- (9) Toda, T.; Igarashi, H.; Uchida, H.; Watanabe, M. *J. Electrochem. Soc.* **1999**, *146*, 3750–3756.
- (10) Mukerjee, S.; Srinivasan, S. *J. Electroanal. Chem.* **1993**, *357*, 201–224.
- (11) Hasché, F.; Oezaslan, M.; Strasser, P. *ChemCatChem* **2011**, *3*, 1805–1813.
- (12) Solla-Gullon, J.; Vidal-Iglesias, F. J.; Feliu, J. M. *Annu. Rep. Prog. Chem., Sect. C: Phys. Chem.* **2011**, *107*, 263–297.
- (13) Koper, M. T. M. *Nanoscale* **2011**, *3*, 2054–2073.
- (14) Shao, M.; Peles, A.; Shoemaker, K. *Nano Lett.* **2011**, *11*, 3714–3719.
- (15) Perez-Alonso, F. J.; McCarthy, D. N.; Nierhoff, A.; Hernandez-Fernandez, P.; Strebel, C.; Stephens, I. E. L.; Nielsen, J. H.; Chorkendorff, I. *Angew. Chem., Int. Ed.* **2012**, *51*, 4641–4643.
- (16) Wang, Y.-J.; Zhao, N.; Fang, B.; Li, H.; Bi, X. T.; Wang, H. *Chem. Rev.* **2015**, *115*, 3433–3467.
- (17) Tian, N.; Zhou, Z.-Y.; Sun, S.-G.; Ding, Y.; Wang, Z. L. *Science* **2007**, *316*, 732–735.
- (18) Stamenkovic, V. R.; Fowler, B.; Mun, B. S.; Wang, G. F.; Ross, P. N.; Lucas, C. A.; Markovic, N. M. *Science* **2007**, *315*, 493–497.
- (19) Gasteiger, H. A.; Markovic, N. M. *Science* **2009**, *324*, 48–49.
- (20) Zhang, J.; Yang, H.; Fang, J.; Zou, S. *Nano Lett.* **2010**, *10*, 638–644.
- (21) Cui, C.; Gan, L.; Li, H. H.; Yu, S. H.; Heggen, M.; Strasser, P. *Nano Lett.* **2012**, *12*, 5885–5889.
- (22) Wu, J.; Qi, L.; You, H.; Gross, A.; Li, J.; Yang, H. *J. Am. Chem. Soc.* **2012**, *134*, 11880–11883.
- (23) Choi, S. I.; Xie, S.; Shao, M.; Odell, J. H.; Lu, N.; Peng, H. C.; Protsailo, L.; Guerrero, S.; Park, J.; Xia, X.; Wang, J.; Kim, M. J.; Xia, Y. *Nano Lett.* **2013**, *13*, 3420–3425.

- (24) Oh, A.; Baik, H.; Choi, D. S.; Cheon, J. Y.; Kim, B.; Kim, H.; Kwon, S. J.; Joo, S. H.; Jung, Y.; Lee, K. *ACS Nano* **2015**, *9*, 2856–2867.
- (25) Gan, L.; Cui, C.; Heggen, M.; Dionigi, F.; Rudi, S.; Strasser, P. *Science* **2014**, *346*, 1502–1506.
- (26) Cui, C.; Gan, L.; Heggen, M.; Rudi, S.; Strasser, P. *Nat. Mater.* **2013**, *12*, 765–771.
- (27) Chen, C.; Kang, Y.; Huo, Z.; Zhu, Z.; Huang, W.; Xin, H. L.; Snyder, J. D.; Li, D.; Herron, J. A.; Mavrikakis, M.; Chi, M.; More, K. L.; Li, Y.; Markovic, N. M.; Somorjai, G. A.; Yang, P.; Stamenkovic, V. R. *Science* **2014**, *343*, 1339–1343.
- (28) Malacrida, P.; Escudero-Escribano, M.; Verdaguier-Casadevall, A.; Stephens, I. E. L.; Chorkendorff, I. *J. Mater. Chem. A* **2014**, *2*, 4234–4243.
- (29) Tan, X.; Prabhudev, S.; Kohandehghan, A.; Karpuzov, D.; Botton, G. A.; Mitlin, D. *ACS Catal.* **2015**, *5*, 1513–1524.
- (30) Loukrakpam, R.; Shan, S.; Petkov, V.; Yang, L.; Luo, J.; Zhong, C.-J. *J. Phys. Chem. C* **2013**, *117*, 20715–20721.
- (31) Shan, S.; Luo, J.; Wu, J.; Kang, N.; Zhao, W.; Cronk, H.; Zhao, Y.; Joseph, P.; Petkov, V.; Zhong, C.-J. *RSC Adv.* **2014**, *4*, 42654–42669.
- (32) Zhang, C.; Sandorf, W.; Peng, Z. *ACS Catal.* **2015**, *5*, 2296–2300.
- (33) Huang, X.; Zhao, Z.; Chen, Y.; Zhu, E.; Li, M.; Duan, X.; Huang, Y. *Energy Environ. Sci.* **2014**, *7*, 2957–2962.
- (34) Wu, Y.; Wang, D.; Chen, X.; Zhou, G.; Yu, R.; Li, Y. *J. Am. Chem. Soc.* **2013**, *135*, 12220–12223.
- (35) Stamenkovic, V. R.; Mun, B. S.; Arenz, M.; Mayrhofer, K. J. J.; Lucas, C. A.; Wang, G.; Ross, P. N.; Markovic, N. M. *Nat. Mater.* **2007**, *6*, 241–247.
- (36) Guo, S.; Li, D.; Zhu, H.; Zhang, S.; Markovic, N. M.; Stamenkovic, V. R.; Sun, S. *Angew. Chem., Int. Ed.* **2013**, *52*, 3465–3468.
- (37) Wang, C.; Wang, G.; Van Der Vliet, D.; Chang, K. C.; Markovic, N. M.; Stamenkovic, V. R. *Phys. Chem. Chem. Phys.* **2010**, *12*, 6933–6939.
- (38) Wang, D.; Xin, H. L.; Hovden, R.; Wang, H.; Yu, Y.; Muller, D. A.; Disalvo, F. J.; Abruña, H. D. *Nat. Mater.* **2012**, *12*, 81–87.
- (39) Wang, C.; Li, D.; Chi, M.; Pearson, J.; Rankin, R. B.; Greeley, J.; Duan, Z.; Wang, G.; Van Der Vliet, D.; More, K. L.; Markovic, N. M.; Stamenkovic, V. R. *J. Phys. Chem. Lett.* **2012**, *3*, 1668–1673.
- (40) Wanjala, B. N.; Loukrakpam, R.; Luo, J.; Njoki, P. N.; Mott, D.; Zhong, C.-J.; Shao, M.; Protsailo, L.; Kawamura, T. *J. Phys. Chem. C* **2010**, *114*, 17580–17590.
- (41) Mukundan, V.; Wanjala, B. N.; Loukrakpam, R.; Luo, J.; Yin, J.; Zhong, C. J.; Malis, O. *Nanotechnology* **2012**, *23*, 335705–335712.
- (42) Wanjala, B. N.; Fang, B.; Loukrakpam, R.; Chen, Y.; Engelhard, M.; Luo, J.; Yin, J.; Yang, L.; Shan, S.; Zhong, C.-J. *ACS Catal.* **2012**, *2*, 795–806.
- (43) Carpenter, M. K.; Moylan, T. E.; Kukreja, R. S.; Atwan, M. H.; Tessema, M. M. *J. Am. Chem. Soc.* **2012**, *134*, 8535–8542.
- (44) Langford, J. I.; Wilson, A. J. C. *J. Appl. Crystallogr.* **1978**, *11*, 102–113.
- (45) Chen, Q.-S.; Solla-Gullón, J.; Sun, S.-G.; Feliu, J. M. *Electrochim. Acta* **2010**, *55*, 7982–7994.
- (46) Vidal-Iglesias, F. J.; Arán-Ais, R. M.; Solla-Gullón, J.; Herrero, E.; Feliu, J. M. *ACS Catal.* **2012**, *2*, 901–910.
- (47) Rudi, S.; Cui, C.; Gan, L.; Strasser, P. *Electrocatalysis* **2014**, *5*, 408–418.